V International Conference on Particle-based Methods – Fundamentals and Applications
PARTICLES 2017
P. Wriggers, M. Bischoff, E. Oñate, D.R.J. Owen, & T. Zohdi (Eds)

VGCM3D - A 3D RIGID PARTICLE MODEL FOR ROCK FRACTURE FOLLOWING THE VORONOI TESSELLATION OF THE GRAIN STRUCTURE: FORMULATION AND VALIDATION

M. CANDEIAS[1], N. MONTEIRO AZEVEDO[2] M. L. BRAGA FARINHA[3]

[1] Laboratório Nacional de Engenharia Civil (LNEC)
Av. do Brasil 101, 1700-066 Lisboa, Portugal
E-mail marilinecandeias@gmail.com, web page: http://www.lnec.pt/organizacao/dbb

[2] Laboratório Nacional de Engenharia Civil (LNEC)
Av. do Brasil 101, 1700-066 Lisboa, Portugal
E-mail nazevedo@lnec.pt, web page: http://www.lnec.pt/organizacao/dbb

[3] Laboratório Nacional de Engenharia Civil (LNEC)
Av. do Brasil 101, 1700-066 Lisboa, Portugal
E-mail lbraga@lnec.pt, web page: http://www.lnec.pt/organizacao/dbb

Key words: Fracture, rock, particle shape, calibration.

Abstract. Detailed particle models by taking into account the material grain structure explicitly consider the material randomness, including a size limiter for damage localization. A VGMC3D contact model is presented that considers the polyhedral particle shape in an approximate way. The VGCM3D flexible contact model is validated against known experimental data on a granite rock, namely triaxial tests and Brazilian tests.

1 INTRODUCTION

Detailed rigid particle models were introduced in the study of fracture of quasi-brittle materials such as concrete, rock and asphalt concrete in the 1990s [1, 2, 3, 4]. More recently, 3D rigid spherical particle models have been proposed both for rock [5, 6, 7, 11] and for concrete, [8, 9, 10].

Particle models are conceptually simpler than a continuum approach, and the development of cracks and rupture surfaces appears naturally as part of the simulation process given its discrete nature. Assemblies of discrete particles connected through simple interaction laws are able to capture the global behaviour of quasi-brittle macro-material, such as concrete or rock. In rock fracture studies the bonded particle model, BPM [6], has received considerable attention given its known ability to model rock complex behaviour, namely in uniaxial compression. The BPM model, as presented in [6], does not match the ratio of the compressive strength to tensile strength that occurs in rock. In addition, the macroscopic friction angle obtained with this model in triaxial testing is much lower than the known hard rock experimental values.

Wang et Tonon [12] proposed a 3D spherical particle model that gives a good agreement with the triaxial failure envelope obtained in Lac du Bonnet granite rock. It is shown that the

inclusion of a frictional term for the contact shear strength has a significant effect in the increase of the macroscopic friction angle. However, the ratio of compressive to tensile strength of Lac du Bonnet granite was not well reproduced. A 3D particle contact model that allows moment transmission at the contact level and adopts a Delaunay 3D edge criteria for particle interaction [7] was presented. This model is shown to be able to predict the failure envelopes and the compressive to tensile strength ratio of a hard rock such as Lac du Bonnet granite. Scholtès and Donzé [11] introduced an interaction range parameter that controls the grain interlock. The particle model proposed by the authors is shown to be able to predict high ratios of tensile to compression strength.

Particle models based on polyhedral particles, either rigid or deformable [13, 14] are computationally more demanding than those based on rigid spherical particles, limiting the number of particles to be modelled or demanding parallelization techniques.

In this paper a 3D rigid particle model is proposed which takes into account the effect of polyhedral shape particles but still keeps the simplicity of spherical particle models and does not require a significant increase in the computational effort. With this purpose, a particle generation algorithm is adopted that generates polyhedral shape particles based on the Laguerre Voronoi diagrams [15]. The Voronoi structure is the dual structure of the weighted Delaunay tetrahedralization of the spherical particle gravity centres. A polyghedral particle model is then approximated by spherical particles that interact with each other through a multiple local contact scheme [7] being the contact area and the contact location given by the common inter-particle Laguerre Voronoi facet. A similar model has been recently proposed for 2D particle models [16]. The model is validated against known results of triaxial and Brazilian tests of a granite rock, showing a good agreement.

FORMULATION

2.1 Fundamentals

In the DEM, the domain is replaced by an assembly of discrete entities that interact with each other through contact points or contact interfaces. The set of forces acting on each particle are related to the relative displacements of the particle with respect to its neighbours. At each step, given the applied forces, Newton's second law of motion is invoked to obtain the new position of the particle. The equations of motion, including local non-viscous damping, of a particle may be expressed as:

$$F_i(t) + F_i^d(t) = m\ddot{x}_i \tag{1}$$

$$M_i(t) + M_i^d(t) = I\dot{\omega}_i \tag{2}$$

where $F_i(t)$ and $M_i(t)$ are, respectively, the total applied force and moment at time t including the exterior contact contribution, m and I are respectively, the particle mass and moment inertia, $\ddot{x}_i$ is the particle acceleration. The damping forces using a local damping formulation are given by:

$$F_i^d(t) = -\alpha|F_i(t)|sign(\dot{x}_i) \tag{3}$$

$$M_i^d(t) = -\alpha|M_i(t)|sign(\omega_i) \tag{4}$$

being $\dot{x}_i$ the particle velocity, ω_i the angular velocity and α the local non-viscous damping parameter and the function $sign(x)$ given by:

$$sign(x) = \begin{cases} +1, & x > 0 \\ -1, & x < 0 \\ 0, & x = 0 \end{cases} \tag{5}$$

2.2 Voronoi-generalized contact model (VGCM-3D)

The 3D Voronoi-generalized contact model (VGCM-3D) is based on the GCM-3D contact model that considers on a given circular surface a discrete number of local contact points that are able to transfer normal and shear forces [7]. Figures 1 a) and b) show the GCM-3D local contact point position for a 4 local contact point scheme. In the VGCM-3D contact model the contact surface and the contact point location are defined by the Voronoi tessellation. The common Voronoi facet is considered to be the contact surface and the vertexes of the Voronoi facet including the gravity centre of the Voronoi facet are considered to be the local contact point location, Figure 1 c) and d). In the GCM-3D contact models, the contact unit normal is defined given the particles centre of gravity and the inter-particle distance:

$$n_i = \frac{x_i^{[B]} - x_i^{[A]}}{d} \tag{6}$$

The contact overlap for the reference contact point and its location, are given by:

$$U^n = R^{[A]} + R^{[B]} - d \tag{7}$$

The VGCM-3D contact model reference contact point, $x_i^{[0]}$, is defined at the associated Voronoi cell facet using:

$$x_i^{[0]} = x_i^{[A]} + \left(R^{[A]} - \frac{1}{2}U^n - d_v\right) n_i \tag{8}$$

where d_v is the distance along the contact normal between the PCM geometric contact plane, Figure 1 a), of the two spherical particles in contact and the adopted contact plane as defined by the corresponding Voronoi cell facet, Figure 1 c).

The local contact point position ($x_i^{[J]}$) in global coordinates is defined relative to the reference local contact point. A local (t, s) axis centred at the reference local contact point is adopted and the relative position of the local points in the local axes, Figures 1 b) and d), are defined at the beginning of the calculation. The contact point position of each local point is then defined in global coordinates using:

$$x_i^{[J]} = x_i^{[0]} + s^{[J]} x_i^{[s]} + t^{[J]} x_i^{[t]} \tag{9}$$

where: $x_i^{[s]}$ and $x_i^{[t]}$ are the local s axes and local t axes, respectively, expressed in global coordinates, assuming that $\vec{s} \times \vec{t} = \vec{n}$. The contact forces that are acting at each local contact

point can be decomposed into its normal and shear component with respect to the contact plane:

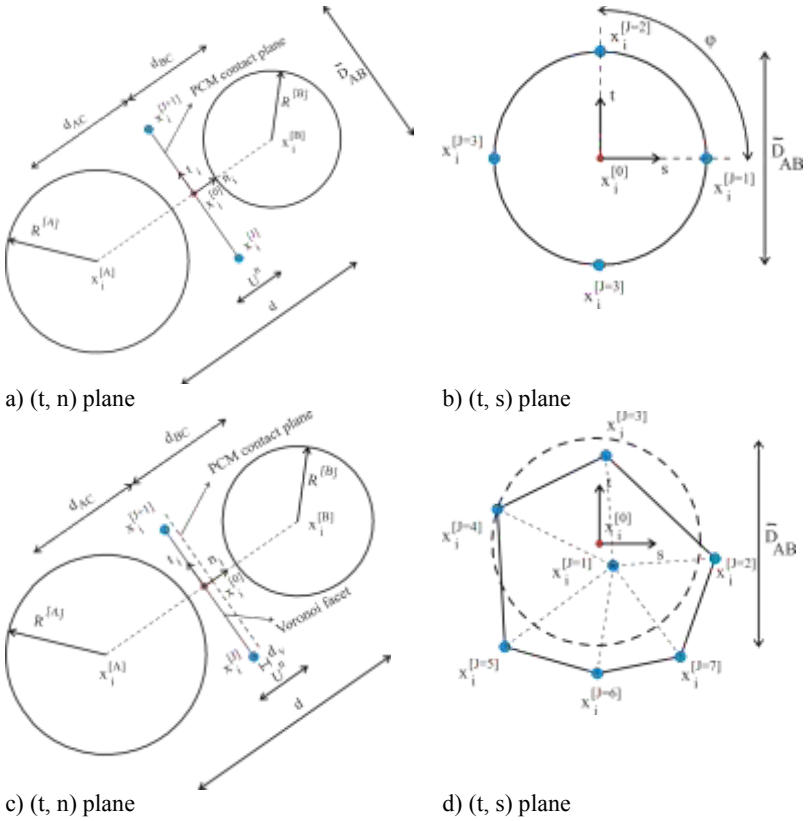

a) (t, n) plane b) (t, s) plane

c) (t, n) plane d) (t, s) plane

Figure 1: GCM-3D contact model with 4 local points considering an approximated circular contact surface a) and b) and VGCM-3D contact model with variable number of local points given by the Voronoi facet vertexes and gravity centre c) and d)

$$F_i^{[J]} = F_i^{[n,J]} + F_i^{[s,J]} \tag{10}$$

The contact velocity of a given local contact point, which is the velocity of particle B relative to particle A, at the contact location is given by:

$$\dot{x}_i^{[J]} = \left(\dot{x}_i^{[J]}\right)_B - \left(\dot{x}_i^{[J]}\right)_A \tag{11}$$
$$= \left(\dot{x}_i^{[B]} + e_{ijk}\omega_j^{[B]}\left(x_k^{[J]} - x_k^{[B]}\right)\right) - \left(\dot{x}_i^{[A]} + e_{ijk}\omega_j^{[A]}\left(x_k^{[J]} - x_k^{[A]}\right)\right)$$

where, e_{ijk} is the permutation tensor. The contact displacement normal increment ($\Delta x^{[J,N]}$) stored as a scalar and shear increment ($\Delta x_i^{[J,S]}$) stored as a vector, are given by:

$$\Delta x^{[J,N]} = \left(\dot{x}_i^{[J]}\Delta t\right)n_i \tag{12}$$

$$\Delta x_i^{[J,S]} = \left(\dot{x}_i^{[J]}\Delta t\right) - \Delta x^{[J,N]}n_i \tag{13}$$

The local contact overlap is defined incrementally for the local points based on the current contact velocity time step (Δt):

$$U^{J,n} = U^{J,n\ old} + \left(\dot{x}_i^{[J]}n_i\right)\Delta t \tag{14}$$

Given the normal and shear stiffness of the local contact point, the normal and shear forces increments are obtained following an incremental linear law:

$$\Delta F^{[J,N]} = -k_n^{[J]}\Delta x^{[J,N]} \tag{15}$$

$$\Delta F_i^{[J,S]} = -k_s^{[J]}\Delta x_i^{[J,S]} \tag{16}$$

The predicted normal and shear contact forces acting at the local contact point are then updated by applying the following equations:

$$F^{[J,N\ new]} = F^{[J,N\ old]} + \Delta F^{[J,N]} \tag{17}$$

$$F_i^{[J,N\ new]} = F_i^{[J,S\ old2]} + \Delta F_i^{[J,S]} \tag{18}$$

Given the predicted normal and shear contact forces the adopted constitutive model is applied, if the predicted forces do not satisfy the constitutive model it is necessary to carry out adjustments. The resultant contact force at the local contact point is then given by:

$$F_i^{[J]} = F^{[J,N]}n_i + F_i^{[J,S]} \tag{19}$$

At the reference contact point the resultant contact force and contact moment are defined given the contribution from all contact points:

$$F_i^{[C]} = \sum_J F_i^{[J]} \tag{20}$$

$$M_i^{[C]} = -\sum_J e_{ijk}(x_j^J - x_j^0)F_k^J \tag{21}$$

The contact force and moment are then transferred to the centre of gravity of each particle in contact through:

$$F_i^{[A]} = F_i^{[A]} - F_i^{[C]} \tag{22}$$

$$F_i^{[B]} = F_i^{[B]} + F_i^{[C]} \tag{23}$$

$$M_i^{[A]} = M_i^{[A]} - e_{ijk}\left(x_j^{[0]} - x_j^{[A]}\right)F_k^{[C]} - M_i^{[C]} \tag{24}$$

$$M_i^{[B]} = M_i^{[B]} + e_{ijk}\left(x_j^{[0]} - x_j^{[B]}\right)F_k^{[C]} + M_i^{[C]} \tag{25}$$

2.3 Numerical stability

When only a steady state solution is sought, a mass scaling algorithm is adopted in order to reduce the number of timesteps necessary to reach the desired solution. The particle mass and inertia are scaled so that the adopted centred-difference algorithm has a higher rate of convergence for a given loading step. The particle scaled mass and inertia used in the calculations are set assuming a unit time increment ($\Delta t = 1$) given the particle stiffness at a given time through:

$$m_{scaled} = 0.25K_t \tag{26}$$

$$I_{scaled} = 0.25K_\theta \tag{27}$$

An upper bound expression for the total particle translation stiffness K_t and of the total rotational stiffness K_θ can be found in [7].

2.4 Local contact stiffness and local contact strength

The VGCM-3D model requires the user definition of the contact deformability parameters, namely the Young's modulus of the equivalent continuum material ($\bar{E}$) and the constant that relates the normal and the shear stiffness spring value (η). In this work the local contact normal and shear stiffness are given by:

$$k_n^{[J]} = \frac{\bar{E}}{d}A_c^{[J]} \tag{28}$$

$$k_s^{[J]} = \eta k_n^{[J]} \tag{29}$$

where, $A_c^{[J]}$ is the contact area associated with the local point J and d is the distance between the particles centre of gravity. In this work the contact geometry is equal to the 3D Voronoi facet [15]. In the VGCM-3D contact model the Voronoi facet is triangulated as indicated in Figure 1 d) and the contact area associated with the local contact point is defined by the sum of one third of the area of the associated triangles.

For the local inter-particle contacts the VGCM-3D model also requires the definition of the contact strength properties, the maximum contact tensile stress ($\sigma_{n.t}$), the maximum contact cohesion stress (τ) and the contact frictional term (μ_c). The maximum contact local tensile strength ($F_{n.max}^{[J]}$) and the maximum local contact shear strength ($F_{s.max}^{[J]}$) are defined given the user-specified contact strength properties and the current local contact normal force ($F_n^{[J]}$) as follows:

$$F_{n.max}^{[J]} = \sigma_{n.t}\, A_c^{[J]} \tag{32}$$

$$F_{s.max}^{[J]} = \tau\, A_c^{[J]} + F_n^{[J]}\, \mu_c = C_{max}^{[J]} + F_n^{[J]}\, \mu_c \tag{33}$$

where $C_{max}^{[J]}$ is the adopted maximum local contact cohesion strength. Figure 2 shows the adopted bilinear softening contact model under tension and shear, more details can be found in [7] regarding the model implementation.

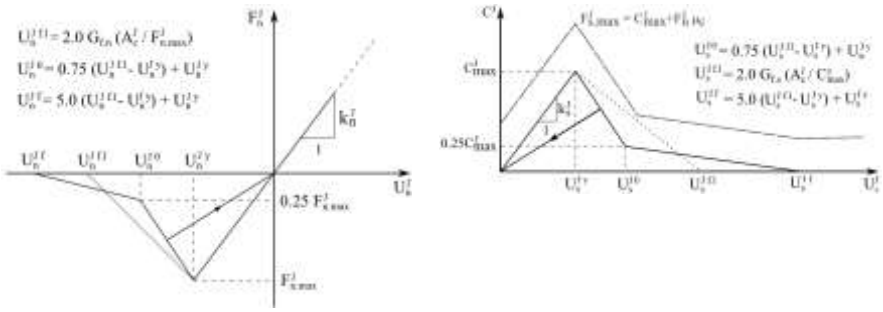

a) Normal direction b) Shear direction

Figure 2: Constitutive model with bilinear softening under tension and shear

2.5 Particle scheme generation

A particle generation scheme has been implemented which generates polyhedral shaped particles based on the Laguerre-Voronoi diagrams [15] using a weighted Delaunay tetrahedralization of the spherical particle gravity centres. A Laguerre tesselation is preferred to a traditional tessellation because it generates Voronoi diagrams with facets closer to the geometric PCM contact planes when considering two particles in contact. The initial particle assembly grain structure is constructed by first introducing spherical particles with half of their radius to ensure that the particles do not overlap with each other, Figure 3 a). Then the real particle radius is adopted, and a DEM cohesionless type solution is obtained, leading to a redistribution of the particle overlap throughout the assembly, Figure 3 b).

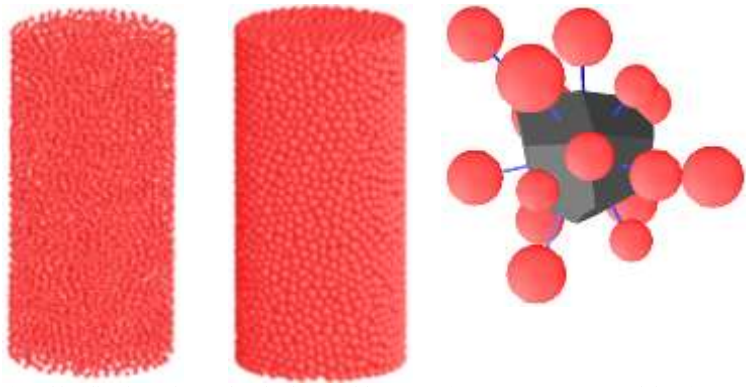

a) Half radius insertion b) Final assembly c) VGCM-3D (Voronoi facet)

Figure 3: VGCM-3D particle assembly and VGCM-3D inter-particle contact

3 TRIAXIAL AND BRAZILIAN TESTS IN A GRANITE ROCK

3.1 Numerical setup

The proposed VGCM-3D model is validated against known uniaxial, triaxial and Brazilian tests in a granite rock [17]. The numerical uniaxial tests, without lateral confinement pressure, and the triaxial tests with lateral confinement pressure are performed in cylindrical specimens with a diameter of 80 mm and a height of 160 mm. The Brazilian tests are performed in cylindrical specimens with a diameter of 80 mm and a thickness of 40 mm. For both geometries, a uniform diameter distribution ranging from 4 to 6 mm was adopted. The uniaxial and triaxial tests assemblies have on average 7988 particles, and the Brazilian tests have on average 1997 particles, Figure 4.

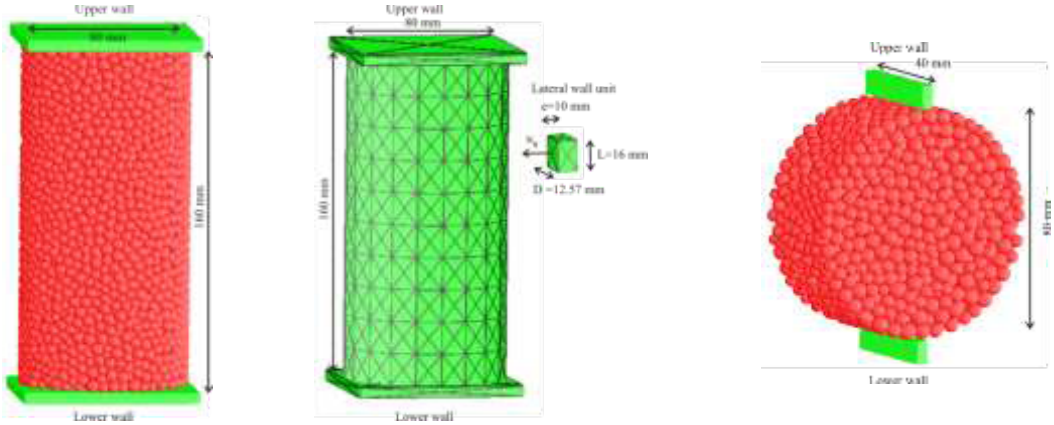

a) Uniaxial test (tensile and compression)

b) Triaxial test

c) Brazilian test

Figure 4: Discrete element model GCM-3D boundary conditions

3.2 Deformability parameters

The influence of the contact deformability parameters, the Young's modulus of the equivalent continuum material ($\bar{E}$) and the constant that relates the shear and normal stiffness spring value (η), on the elastic macroscopic properties, Young's modulus (E) and Poisson's coefficient (ν), are assessed. Two sets of tests were carried out. In the first set of tests the macro-properties were obtained by fixing constant values of $\bar{E}$ ($0.5\bar{E}$, $1.0\bar{E}$ and $2.0\bar{E}$) and varying the ratio of normal to shear stiffness. In the second set of tests the macro-properties were obtained by fixing constant values of η (0.0, 0.25, 0.50, 0.75 and 1.0) and varying the elastic contact constant $\bar{E}$. Assuming a $\bar{E}$ value equal to 48.8 GPa.

Figure 5 a) and c) shows that the material Young's modulus is related to both elastic contact model parameters, being more influenced by the ratio of normal to shear stiffness (η) for higher elastic contact values ($\bar{E}$). Figure 5 b) and d) shows that the material Poisson's coefficient is mainly influenced by the ratio of normal to shear stiffness. Similar results were found in [7, 12].

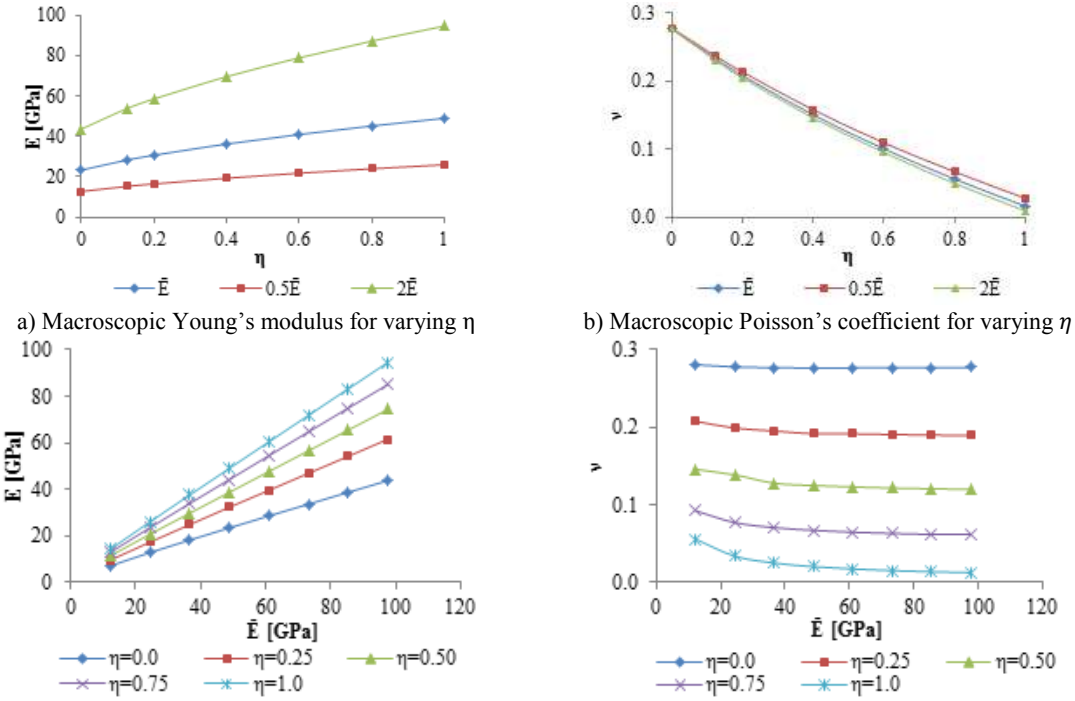

a) Macroscopic Young's modulus for varying η

b) Macroscopic Poisson's coefficient for varying η

c) Macroscopic Young's modulus for varying $\bar{E}$

d) Macroscopic Poisson's coefficient for varying $\bar{E}$

Figure 5: VGCM3D influence of the contact deformability parameters ($\bar{E}$ and η) on the elastic macroscopic properties (ν)

3.3 Calibrated brittle and bilinear softening models

The VGCM-3D with a brittle contact force displacement model (VGCM-3D G_{el}) and the VGCM-3D with a contact force model following a bilinear softening model (VGCM-3D $9.5G_{el}$) were calibrated in order to achieve the set of deformability and strength parameters that predicts numerical results closer to Augig granite experimental data. For the VGCM-3D $9.5G_{el}$, a contact fracture energy equal to 9.5 times the energy of the fracture branch was adopted in tension and shear. In the VGCM-3D G_{el} brittle model the contact energy adopted in tension and shear directions corresponds to the fracture energy associated with the elastic branch.

Table 1 summarizes the micro-properties adopted for each contact model and Table 2 presents the known macroproperties of the Augig Granite and the macroscopic numeric response. Figure 6 shows the strength envelope obtained with the VGCM-3D G_{el} and with the VGCM-3D $9.5G_{el}$ contact models. For both models, the vertical maximum stress-strain values with $0,\ 3, 6, 9$ and 12 MPa confinement pressures are presented. In the presented strength envelope, the plotted tensile strength values correspond to the indirect tensile strength values.

As shown in Table 2 and in Figure 6, the VGCM-3D particle model here proposed is capable of representing the failure envelope and the compressive to tensile strength ratio of a hard rock such as Augig granite. Further, it is shown that by including a bilinear softening law at the contact level (VGCM-3D $9.5G_{el}$), the particle model here presented is capable of predicting a direct tensile to indirect tensile ratio closer to that expected in rock (the indirect tensile strength is usually higher than the direct tensile strength value).

Table 1 – Calibrated Micro-properties adopted in VGCM-3D particle models

	$\bar{E}$ $[GPa]$	η	μ_c	$\sigma_{n.t}$ $[MPa]$	$\tau\ [MPa]$	$G_{f.n}$ $[N/m]$	$G_{f.s}$ $[N/m]$
VGCM-3D G_{el}	48.8	0.125	0.05	35.5	106.5	6.8	3275.2
VGCM-3D $9.5G_{el}$				11.4	88.5	64.6	3114.4

Table 2 - Augig granite macro-properties and numerical macro-properties

	E $[GPa]$	ν	q_u $[MPa]$	$\sigma_{t.dir}$ $[MPa]$	$\sigma_{t.ind}$ $[MPa]$	c $[MPa]$	φ [°]
Augig granite [17]	25.8	0.23	122.1	-	8.8	21.0	53.0
VGCM-3D G_{el} calibrated	25.8	0.23	125.2	16.4	8.9	27.1	43.2
VGCM-3D $9.5G_{el}$ calibrated			124.5	7.4	9.1	24.8	46.6

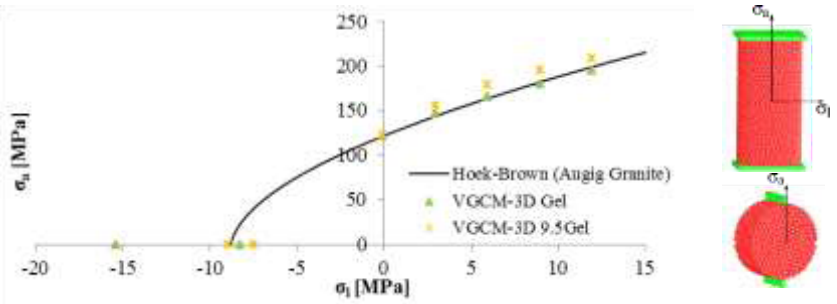

Figure 6: Strength Envelope: VGCM-3D G_{el} and VGCM-3D $9.5G_{el}$ contact models

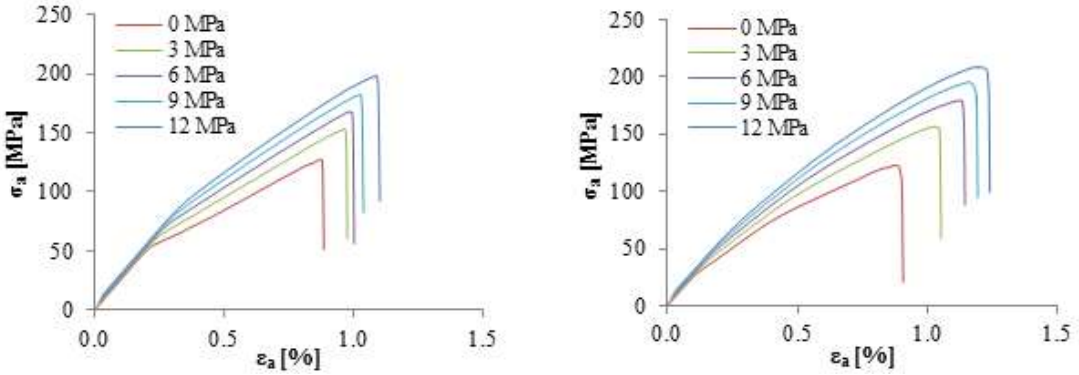

a) VGCM-3D G_{el} calibrated b) VGCM-3D $9.5G_{el}$ calibrated

Figure 7: Vertical stress-strain curves for the different confinement pressures

Figure 7 shows the axial stress–strain response for the uniaxial and the triaxials tests obtained with the VGCM-3D calibrated models for a lateral confinement of 3, 6, 9 and 12 MPa. As shown in Figure 7 the consideration of a bilinear softening law in tension and shear does not lead to an unrealistic ductile macroscopic response. It is verified that the GCM-3D G_{el} calibrated has an extremely brittle response, presenting an inflection point in the stress-strain curves. This inflection point reveals an unexpected loss in the material strength for

stress values lower than the ultimate vertical stress values. This behaviour is more pronounced for lower lateral confinement pressures (0 and 3 MPa). The increase in the lateral confinement pressures increases the ductility of the stress-strain curves. Comparing both models, the stress-strain curves obtained with the GCM-3D $9.5G_{el}$ calibrated model have a less brittle response when compared to the stress-strain curves obtained with the GCM-3D G_{el} calibrated model.

Figure 8 shows the crack patterns obtained in uniaxial compression, direct tensile, triaxial with confinement stress of 9 MPa and in an indirect tensile test (Brazilian) for the VGCM-3D $9.5G_{el}$ calibrated model. As can be seen, the crack patterns obtained for the different tests are accordingly to the expected. In the uniaxial compression test without friction between the horizontal walls and the particle assembly the development of vertical cracks, Figure 8 a). The increase of confinement stress leads to a development of shear surfaces with a given inclination, as observed in Figure 8 c). In the direct tensile test the rupture surface is perpendicular to the load direction, and in the indirect tensile test the rupture surface is parallel to the load direction.

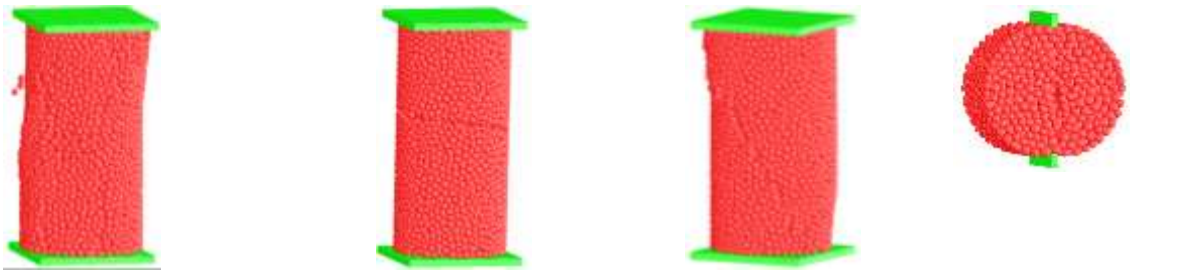

a) Uniaxial compression test b) Direct tensile test c) $\sigma_1 = 9$ MPa d) Brazilian test

Figure 8: VGCM-3D $9.5G_{el}$ calibrated final fracture patterns

4 CONCLUSIONS

A generalized 3D contact model, VGCM-3D, which enables moment transmission and contact discretizations with multiple local contact points is presented. The contact geometry and location are given by the Laguerre–Voronoi diagram facets, and the neighbouring particles are considered to interact if a common Voronoi facet is shared. By incorporating the VGCM-3D as described, the rigid particle model takes into account the polyhedral shaped particles in an approximate way, but still keeps the simplicity of spherical particle models and does not require a significant increase in the computational effort.

The results presented highlight the need to incorporate a bilinear softening constitutive model at the contact level to obtain a better agreement between the direct tensile strength and the indirect tensile strength. The latter ratio cannot be correctly predicted with a simple brittle model. It is also shown that particle assemblies with bilinear softening contact laws still predict a brittle macroscopic response under tensile, compression and biaxial state of stress. The bilinear contact model, for the level of contact fracture energy adopted, does not change significantly the fracture processes, it mainly slows down the rupture evolution and slightly induces a higher localization of the final crack patterns.

Finally the model shows a good agreement with known results of triaxial and Brazilian tests of a granite rock.

REFERENCES

[1] Meguro, K., Iwashita, K. and Hakuno, M. Fracture analyses of media composed of irregularly shaped regions by the extended distinct element method. *Structural Eng./Earthquake Eng.,* (1991) **8 (3)**:37-48.

[2] Potyondy, D., Cundall, P. and Lee C. Modelling rock using bonded assemblies of circular particles. In: Aubertin M. et al (eds) Proceedings of the 2nd North American Rock Mechanics Symposium, Rotterdam, Balkema, (1996), 1937-1944 .

[3] Schlangen, E. and Garboczi, E. Fracture simulation of concrete using lattice models: Computational aspects. *Engineering Fracture Mechanics,* (1997) **57(2/3)**:319-332.

[4] Chang, K.G. and Meegoda, J.N. Micromechanical simulation of hot mix asphalt. *Journal of Engineering Mechanics. ASCE.* (1997), 123(5):495-503.

[5] Matsuda, Y. and Iwase, Y. Numerical simulation of rock fracture using three-dimensional extended discrete element method. Earth Planets Space, (2002), **54(4)**: 367:378.

[6] Potyondy, D. and Cundall, P. A bonded-particle model for rock. *International Journal of Rock mechanics and Mining Sciences,* (2004) **41(8)**: 1329-1364.

[7] Monteiro Azevedo, N. and Lemos, J. A 3D generalized rigid particle contact model for rock fracture. *Engineering Computations*, (2013), **30(2)**:277-300.

[8] Lilliu, G. and Van Mier, M. 3D lattice type fracture model for concrete. *Engineering Fracture Mechanics*, (2003) **70(7-8)**:927-941.

[9] Hentz, S., Daudeville, L., Donzé, F.V. Identification and validation of a discrete element model for concrete. *Journal of Engineering Mechanics. ASCE.* (2004), **130(6)**:709-719.

[10] Cusatis, P., Bazant, Z. and Cedolin, L. Confinement-shear lattice CSL model for fracture propagation in concrete. *Computer Methods in Applied Mechanics and Engineering,* (2006) **195(52)**:7154-7171.

[11] Scholtès, L. and Donzé, F.V. A DEM model for soft and hard rocks: Role of grain interlocking. *Journal of the Mechanics and Physics of Solids.* (2013), **61(2)**:709-719.

[12] Wang, Y. and Tonon, F. Modeling Lac du Bonnet granite using a discrete element model. *International Journal of Rock mechanics and Mining Sciences*, (2009), **46(7)**: 1124:1135.

[13] Gao, F. and Stead, D., The application of a modified Voronoi logic to brittle fracture modelling at the laboratory and field scale. *International Journal of Rock Mechanics and Mining Sciences*, (2014), **68**: 1:14.

[14] Ghazvinian, E., Diederichs, M. and Quey, R., 3D Random Voronoi grain-based models for simulation of brittle rock damage and fabric-guided micro-fracturing. *Journal of Rock Mechanics and Geotechnical Engineering*, (2014), **6(6)**: 506:521.

[15] Okabe, A., Boots, B. and Sugihara, K. *Spatial tesselations. Concepts and applications of Voronoi diagrams*, John Wiley & Sons (1992).

[16] Monteiro Azevedo, N., Candeias, M. and Gouveia, F., A rigid particle model for rock fracture following the Voronoi tessellation of the grain structure: Formulation and Validation, *Rock mechanics and Rock Engineering,* (2015), **48(2)**:535-557.

[17] Kazerani, T. and Zhao, J. Micromechanical parameters in bonded particle method for modelling of brittle material failure, *International Journal for Numerical and Analytical Methods in Geomechanics*, (2010), **34(18)**:1877-1895.